



Analysis of material susceptibility in silicon on insulator waveguides with combined simulation of four-wave mixing and linear mode coupling

Ulrike Höfler¹ · Tasnad Kernetzky¹ · Norbert Hanik¹

Received: 31 October 2021 / Accepted: 12 July 2022 / Published online: 22 October 2022
© The Author(s) 2022

Abstract

We derive propagation equations modeling third-order susceptibility-induced nonlinear interaction and linear mode coupling in waveguides. We model material susceptibility with Raman and electronic response which include approximations suited for optical communications. We validate our model by comparing numerical integration of the propagation equations to continuous wave measurements of a silicon on insulator waveguide.

Keywords Nonlinear optics · Susceptibility · Four-wave mixing · Silicon nano-rib waveguide

1 Introduction

All-optical signal processing is a promising technique for various applications. Two prominent examples are optical phase conjugation (OPC) for mitigating nonlinear impairments in optical fiber links (Vukovic et al. 2015) and wavelength conversion (WLC) which shows high potential for several scenarios. In a narrowband sense, WLC can enable all-optical routing in datacenters or metropolitan networks. In a broadband sense, WLC allows to jointly multiplex several fully-loaded C-bands into one fiber by shifting them to distinct bands. Different approaches based on highly non-linear fibers (Rademacher et al. 2020), LiNbO³ waveguides (Minzioni et al. 2010), and silicon on insulator (SOI) waveguides (Gajda et al. 2018; Ronniger et al. 2020) have been investigated. We present a simulation for the latter, including

Guest editors: Slawek Sujecki, Asghar Asgari, Donati Silvano, Karin Hinzer, Weida Hu, Piotr Martyniuk, Alex Walker and Pengyan.

✉ Ulrike Höfler
ulrike.hoefler@tum.de

Tasnad Kernetzky
tasnad.kernetzky@tum.de

Norbert Hanik
norbert.hanik@tum.de

¹ Technical University of Munich, Munich, Germany

nonlinear effects and linear mode coupling, with an accurate model of the susceptibility in silicon.

Third-order material nonlinearity—the origin of four-wave mixing (FWM)—is the basis for all-optical signal processing. Due to the high nonlinear potential of silicon, the application of an SOI waveguide demands a more detailed consideration of nonlinearity than it is provided by the optical nonlinear Schrödinger equation. Therefore, we derive a set of coupled differential equations that model linear and nonlinear interaction based on the third-order susceptibility (resembling pulse propagation in Agrawal (2013)). As a result of the high Raman gain coefficient in silicon—which is three to four orders of magnitude higher compared to silica (Jalali et al. 2006)—it is essential to include the effect of molecular vibrations (Raman response) besides the commonly considered electron vibrations (Kerr effect).

The input-output conversion efficiency (CE) defined as idler output power over signal input power is a critical measure of the nonlinear process’s performance. For achieving a strong idler build-up, phase matching (PM) has to be performed and multi-mode operation is usually preferred since an additional degree of freedom is obtained. We refer to Kernetzky et al. (2020) for a detailed analysis of geometry optimization for PM in SOI waveguides. In Höfler et al. (2021) we described a model for the susceptibility calculation in silicon. This is extended in this work by applying the susceptibility model to the propagation equations of an SOI waveguide, as well as by comparing the results to a continuous wave measurement of the waveguide.

2 Modeling light propagation

For investigating the spatial development of the amplitudes of the interacting frequencies along the waveguide, the corresponding differential equations will be stated, starting from the wave equation

$$\Delta \vec{E} - \nabla (\nabla \cdot \vec{E}) = \mu_0 \partial_t^2 \vec{D}. \tag{1}$$

The electric displacement field is defined as

$$\vec{D} = \epsilon_0 \cdot (\epsilon_r \vec{E} + \vec{P}^{nl}), \tag{2}$$

where the extended material permittivity matrix

$$\epsilon_r = \epsilon'_r \mathbf{I} + \delta \epsilon_r - j \epsilon''_r \mathbf{I} \tag{3}$$

models material dispersion by $\epsilon'_r(x, y) = n^2(x, y)$, linear perturbations by the matrix $\delta \epsilon_r(x, y, z)$, light attenuation by $\epsilon''_r(x, y)$, and where \mathbf{I} is the identity matrix. Rearranging all perturbations into one vector yields

$$\vec{D} = \epsilon_0 \cdot (\epsilon'_r \vec{E} + \vec{P}') \tag{4}$$

with $\vec{P}' = \delta \epsilon_r \vec{E} - j \epsilon''_r \vec{E} + \vec{P}^{nl}$. Inserting \vec{D} in Eq. 1 gives

$$\Delta \vec{E} + \nabla \left(\underbrace{\frac{1}{\epsilon'_r} \cdot (\vec{E} \nabla \epsilon'_r + \nabla \cdot \vec{P}')}_{\text{A}} \right) - \mu_0 \epsilon_0 \epsilon'_r \partial_t^2 \vec{E} = \mu_0 \epsilon_0 \partial_t^2 \vec{P}'. \tag{5}$$

We model the nonlinear polarization vector as

$$\vec{P}^{nl} = \iiint \overset{\leftrightarrow}{\chi}^{[3]}(\tau_\zeta, \tau_\eta, \tau_\rho) : \vec{E}(t - \tau_\zeta) \vec{E}(t - \tau_\eta) \vec{E}(t - \tau_\rho) d\tau_\zeta d\tau_\eta d\tau_\rho, \tag{6}$$

which contains the susceptibility tensor $\overset{\leftrightarrow}{\chi}^{[3]} \in \mathbb{C}^{3 \times 3 \times 3 \times 3}$, and where $:$ represents the tensor product. Stating Eq. 6 in sum-notation gives

$$P_i^{nl} = \iiint \sum_{j,k,l} \chi_{ijkl}^{[3]}(\tau_\zeta, \tau_\eta, \tau_\rho) \cdot E_j(t - \tau_\zeta) \cdot E_k(t - \tau_\eta) \cdot E_l(t - \tau_\rho) d\tau_\zeta d\tau_\eta d\tau_\rho \tag{7}$$

with $i, j, k, l \in \{x, y, z\}$.

The unmodulated total propagating electrical field can be written as a superposition of modes (m) at discrete positive frequencies f_i

$$\vec{E} = \Re \left\{ \sum_{i,m} \vec{E}_{f_i}^{(m)} \right\} = \frac{1}{2} \sum_{i,m} \hat{E}_{f_i}^{(m)} \vec{\Psi}_{f_i}^{(m)} e^{j(2\pi f_i t - \beta_{f_i}^{(m)} z)} + c.c., \tag{8}$$

with real part $\Re\{\cdot\}$, amplitudes $\hat{E}_{f_i}^{(m)}(z) \in \mathbb{C}$, transversal field distributions $\vec{\Psi}_{f_i}^{(m)}(x, y)$, and propagation constants $\beta_{f_i}^{(m)}$. In the following, we make the common assumption that \vec{P}' causes a z -dependence of \hat{E} , but does not have any effect on $\vec{\Psi}$. Since the outer gradient in term \textcircled{A} in Eq. 5 alters the transversal field profiles, $\nabla \cdot \vec{P}' = 0, \forall \vec{P}'$ has to hold to fulfill the assumption that \vec{P}' does not affect $\vec{\Psi}$. With that, evaluating Eq. 5 at the positive frequency f_0 (analytic signal) leads to

$$\Delta \vec{E} + \nabla \left(\frac{1}{\epsilon'_r} \vec{E} \nabla \epsilon'_r \right) - \mu_0 \epsilon_0 \epsilon'_r \partial_t^2 \vec{E} = \mu_0 \epsilon_0 \partial_t^2 \vec{P}', \tag{9}$$

with $\vec{P}' := \vec{P}'|_{+f_0}$ and $\vec{E} := \vec{E}|_{+f_0}$.

After quite some calculus, algebra and by assuming $\partial_z \epsilon'_r = 0$, the x component of Eq. 9 becomes

$$\begin{aligned} & \sum_m \left[\underbrace{\left\{ \left(\partial_x^2 + \partial_y^2 \right) \Psi_{x,f_0}^{(m)} + \left(\epsilon'_r \beta_0^2 - \beta_{f_0}^{(m)2} \right) \cdot \Psi_{x,f_0}^{(m)} \partial_x \left[\frac{1}{\epsilon'_r} \cdot \left(\Psi_{x,f_0}^{(m)} \partial_x \epsilon'_r + \Psi_{y,f_0}^{(m)} \partial_y \epsilon'_r \right) \right] \right\}}_{\textcircled{B}} \cdot \hat{E}_{f_0}^{(m)} e^{j(2\pi f_0 t - \beta_{f_0}^{(m)} z)} \right. \\ & \left. + \left(\partial_z^2 \hat{E}_{f_0}^{(m)} - 2j\beta_{f_0}^{(m)} \partial_z \hat{E}_{f_0}^{(m)} \right) \Psi_{x,f_0}^{(m)} e^{j(2\pi f_0 t - \beta_{f_0}^{(m)} z)} \right] \\ & = 2\mu_0 \epsilon_0 \partial_t^2 \mathcal{P}'_x \end{aligned} \tag{10}$$

with $\beta_0 = 2\pi f_0 / c_0$. Since the field amplitude $\hat{E}_{f_0}^{(m)}(z)$ only changes due to perturbations \vec{P}' , all addends with $\partial_z \hat{E}$ vanish in the homogeneous equation ($\vec{P}' = \vec{0}$). This indicates that due to mode orthogonality all m summands needs to be equal to zero, i.e., $\textcircled{B} = 0 \forall m$. Based on the assumption that \vec{P}' does not alter $\vec{\Psi}$, this also has to hold for $\vec{P}' \neq \vec{0}$. Consequently, by extending Eq. 10 by the y and z component one gets

$$\sum_m -j\beta_{f_0}^{(m)} \partial_z \left(\hat{E}_{f_0}^{(m)} \right) \cdot \vec{\Psi}_{f_0}^{(m)} e^{j(2\pi f_0 t - \beta_{f_0}^{(m)} z)} = \mu_0 \epsilon_0 \partial_t^2 \vec{P}', \tag{11}$$

which also makes use of the slowly varying wave approximation $\left| \partial_z^2 \hat{E}_{f_0}^{(m)} \right| \ll \left| 2\beta_{f_0}^{(m)} \partial_z \hat{E}_{f_0}^{(m)} \right|$, as well as $\left| \partial_z \hat{E}_{f_0}^{(m)} \right| \ll \left| \beta_{f_0}^{(m)} \hat{E}_{f_0}^{(m)} \right|$ for the z component.

The nonlinear part of $\vec{\mathcal{P}}'$ is governed by the third-order material susceptibility $\overset{\leftrightarrow}{\chi}^{[3]}$. This tensor generates a nonlinear perturbation at frequency f_0 by combining three interacting light waves. Inserting Eq. 8 into Eq. 6 and only considering frequency combinations $(f_\zeta, f_\eta, f_\rho)$ with two positive and one negative contribution (thus, considering processes such as OPC and Bragg scattering (BS)) gives

$$\begin{aligned} \bar{p}^{\text{nl}}|_{+f_0} &= \sum_{(\zeta, \eta, \rho) \in \mathcal{S}} \sum_{(m_1, m_2, m_3) \in \mathcal{M}} \frac{3}{8} \hat{E}_{f_\zeta}^{(m_1)} \hat{E}_{f_\eta}^{(m_2)*} \hat{E}_{f_\rho}^{(m_3)} \cdot \overset{\leftrightarrow}{\mathcal{X}}^{[3]}(f_\zeta, f_\eta, f_\rho) : \bar{\Psi}_{f_\zeta}^{(m_1)} \bar{\Psi}_{f_\eta}^{(m_2)*} \bar{\Psi}_{f_\rho}^{(m_3)*} e^{j(2\pi f_0 t - \delta\beta z)}, \\ \mathcal{S} &= \{(\zeta, \eta, \rho) : f_0 = f_\zeta + f_\eta + f_\rho \mid f_{\zeta, \rho} > 0, f_\eta < 0\}, \\ \mathcal{M} &= \{(m_1, m_2, m_3) \mid m_{1,2,3} \in \{\text{TE}_0, \text{TE}_1, \dots\}\}, \\ \delta\beta &= \beta_{f_\zeta}^{(m_1)} - \beta_{f_\eta}^{(m_2)} + \beta_{f_\rho}^{(m_3)}, \end{aligned} \tag{12}$$

where $\overset{\leftrightarrow}{\mathcal{X}}^{[3]}$ is the Fourier transform of $\overset{\leftrightarrow}{\chi}^{[3]}$, i.e., $\mathcal{F}\{\overset{\leftrightarrow}{\chi}^{[3]}\} = \overset{\leftrightarrow}{\mathcal{X}}^{[3]}$.

Inserting Eq. 12 in Eq. 11, multiplying with $\bar{\Psi}_{f_0}^{(a)*}$ from the left and integrating over the cross section (making use of mode orthogonality), we obtain the propagation equation for mode (a) at frequency f_0

$$\begin{aligned} \partial_z \hat{E}_{f_0}^{(a)} &= - \underbrace{\frac{\alpha^{(a)}}{2}}_{\text{attenuation}} \hat{E}_{f_0}^{(a)} - j\tilde{\gamma} \sum_m \underbrace{C_{(m)}^{(a)}}_{\text{mode coup.}} \hat{E}_{f_0}^{(m)} e^{-j\Delta\beta_{\text{lin}} z} \\ &\quad - j \frac{3\tilde{\gamma}}{4} \sum_{(\zeta, \eta, \rho) \in \mathcal{S}} \sum_{(m_1, m_2, m_3) \in \mathcal{M}} \underbrace{N_{(m_1, m_2, m_3)}^{(a)}}_{\text{nonlin. coefficient}} \cdot \hat{E}_{f_\zeta}^{(m_1)} \hat{E}_{f_\eta}^{(m_2)*} \hat{E}_{f_\rho}^{(m_3)} e^{-j\Delta\beta z}, \end{aligned} \tag{13}$$

with

$$\begin{aligned} \Delta\beta_{\text{lin}} &= \beta_{f_0}^{(m)} - \beta_{f_0}^{(a)}, & \tilde{\gamma} &= \frac{\beta_0^2}{2\beta_{f_0}^{(a)} \iint |\bar{\Psi}_{f_0}^{(a)}|^2 dA}, \\ \Delta\beta &= \beta_{f_\zeta}^{(m_1)} - \beta_{f_\eta}^{(m_2)} + \beta_{f_\rho}^{(m_3)} - \beta_{f_0}^{(a)}, & \alpha^{(a)} &= \frac{\beta_0^2 \epsilon_f''}{\beta_{f_0}^{(a)}}, \\ C_{(m)}^{(a)} &= \iint \bar{\Psi}_{f_0}^{(a)*} \delta\epsilon_f \bar{\Psi}_{f_0}^{(m)} dA, & N_{(m_1, m_2, m_3)}^{(a)} &= \iint \bar{\Psi}_{f_0}^{(a)*} \cdot \overset{\leftrightarrow}{\mathcal{X}}^{[3]}(f_\zeta, f_\eta, f_\rho) : \bar{\Psi}_{f_\zeta}^{(m_1)} \bar{\Psi}_{f_\eta}^{(m_2)*} \bar{\Psi}_{f_\rho}^{(m_3)*} dA. \end{aligned} \tag{14}$$

The mode coupling (MC) coefficient $C_{(m)}^{(a)}$ couples modes at the same frequency whereas the nonlinearity coefficient $N_{(m_1, m_2, m_3)}^{(a)}$ couples between modes at all possible frequency combinations. This leads to a set of coupled differential equations of the type of Eq. 13 which has to be solved numerically. While the source fields can propagate in different modes and at arbitrary frequencies, the efficiency of the linear and nonlinear processes is determined by energy conservation and by the phase mismatches $\Delta\beta_{\text{lin}}$ and $\Delta\beta$, respectively.

3 Susceptibility in silicon

In the following, the third-order susceptibility for silicon as origin of nonlinear effects is analyzed. In silicon, there are two main parts that account for nonlinear processes, namely

the electronic contribution (e) due to bound electrons and the Raman contribution (R) stemming from atomic lattice vibrations. Hence, it is reasonable to split the third-order nonlinear susceptibility tensor into its main parts, i.e., $\overset{\leftrightarrow}{\chi}^{[3]} = \overset{\leftrightarrow}{\chi}_e + \overset{\leftrightarrow}{\chi}_R$, and investigate each part separately (Lin et al. 2007). Throughout this section, we assume a waveguide fabricated on a (001) surface and parallel to the [110] direction.

3.1 Electronic susceptibility in frequency domain

Due to spatial symmetry, only 21 out of 81 entries of $\overset{\leftrightarrow}{\chi}_e$ are nonzero, of which four are independent of each other (Boyd 2003). If only wavelengths $\lambda > \lambda_{\min} = 1.10 \mu\text{m}$ are considered, the Kleinmann condition is satisfied and three of the four independent elements can be approximated to be equal (Lin et al. 2007; Bristow et al. 2007; Osgood et al. 2009). Usually the electronic susceptibility is considered as nearly constant, since variations of the interacting frequencies lead to only small fluctuations of $\overset{\leftrightarrow}{\chi}_e$. For a wavelength range including the commonly used optical bands from O to L, the spacing between interacting frequencies is small enough to treat nonlinearity caused by the electronic contribution as being independent of the interacting frequencies, i.e., $\overset{\leftrightarrow}{\chi}_e(f_0; f_\zeta, f_\eta, f_\rho) \approx \overset{\leftrightarrow}{\chi}_e(f_0)$. With this assumption and for $\lambda \in [1.2 \mu\text{m}, 2.4 \mu\text{m}]$ (also including bands O to L), the last two independent entries of $\overset{\leftrightarrow}{\chi}_e$ can be related to each other as well (Zhang et al. 2007). Furthermore, the real and imaginary part of the last independent entry is linked to the Kerr coefficient n_2 and the two-photon absorption coefficient β_{tpa} , respectively. Altogether, this leads to the 21 nonzero elements

$$\begin{aligned}
 X_e^{xxxx} &= \Re\{X_e^{xxxx}\} + j\Im\{X_e^{xxxx}\} \\
 &= X_e^{yyyy} = X_e^{zzzz}, \\
 \frac{X_e^{xxxx}}{2.36} &= X_e^{xyyy} = X_e^{zzyy} = X_e^{yyzz} = X_e^{zzxx} = X_e^{xxzz} \\
 &= X_e^{yyxx} = X_e^{xyxy} = X_e^{zyzy} = X_e^{yzyz} = X_e^{zxzx} \\
 &= X_e^{xzxz} = X_e^{yxxy} = X_e^{xyyx} = X_e^{zyyz} = X_e^{yzzz} \\
 &= X_e^{zzxz} = X_e^{yxxz} = X_e^{xzzx},
 \end{aligned} \tag{15}$$

with $\Re\{X_e^{xxxx}\} = 2.3482 \cdot n_2(f_0) \cdot \epsilon_0 \cdot c_0 \cdot n^2(f_0)$, $\Im\{X_e^{xxxx}\} = \frac{1.1741}{2\pi f_0} \cdot \beta_{\text{tpa}}(f_0) \cdot \epsilon_0 \cdot c_0^2 \cdot n^2(f_0)$ (Osgood et al. 2009; Hon et al. 2011), where the characteristics of n_2 and β_{tpa} can be found in Bristow et al. (2007).

3.2 Raman susceptibility in frequency domain

The Raman contribution $\overset{\leftrightarrow}{\chi}_R$ emerges from the interaction of light with lattice vibrations (phonons) of the material. If the difference of two incident light waves coincides with the frequency of the lattice vibration (resonance), the atom is excited to a higher vibrational eigenstate. The susceptibility elements induced by Raman scattering can be stated as Dim-

itropoulos et al. (2003); Jalali et al. (2006); Lin et al. (2007)

$$\begin{aligned}
 X_R^{ijkl}(f_0; f_\zeta, f_\eta, f_\rho) &= X_R^{ijkl}(f_0; f_1, -f_2, f_3) \\
 &= \frac{1}{\pi} \cdot f_v \cdot \Gamma \cdot \frac{c_0}{Z_0} \cdot \\
 &\quad \left(X_1^{ijkl}(f_2 - f_3) \cdot \sum_{n=1}^3 (R_{ij})_n \cdot (R_{kl})_n + X_1^{ijkl}(f_2 - f_1) \cdot \sum_{n=1}^3 (R_{il})_n \cdot (R_{jk})_n \right),
 \end{aligned}
 \tag{16}$$

with $\{f_0, f_1, f_2, f_3\} > 0$, $X_1^{ijkl}(f_2 - f_a) = \frac{n^2(f_a) \cdot g_R(f_a)}{f_a \cdot [(f_v^2 - (f_2 - f_a)^2) - j\Gamma \cdot (f_2 - f_a)]}$, $a \in \{1, 3\}$, and $i, j, k, l \in \{x, y, z\}$, where $\Gamma = 105$ GHz is the FWHM-bandwidth, $f_v = 15.6$ THz the vibrational eigenstate frequency, $Z_0 = \sqrt{\frac{\mu_0}{\epsilon_0}}$, g_R the Raman gain coefficient, and R_n , $n \in \{1, 2, 3\}$ the three Raman matrices with

$$R_1 = \frac{1}{\sqrt{2}} \begin{bmatrix} 0 & 0 & -1 \\ 0 & 0 & -1 \\ -1 & -1 & 0 \end{bmatrix}, \quad R_2 = \begin{bmatrix} -1 & 0 & 0 \\ 0 & 1 & 0 \\ 0 & 0 & 0 \end{bmatrix}, \quad R_3 = \frac{1}{\sqrt{2}} \begin{bmatrix} 0 & 0 & 1 \\ 0 & 0 & -1 \\ 1 & -1 & 0 \end{bmatrix}.$$

Each Raman matrix corresponds to the respective displacement of the phonons along the crystallographic directions of the medium and reflects its crystal symmetry. The terms $\sum_{n=1}^3 (R_{ij})_n \cdot (R_{kl})_n$ and $\sum_{n=1}^3 (R_{il})_n \cdot (R_{jk})_n$ determine the 18 nonzero elements of \vec{X}_R . All denoted frequency values apply only at room temperature, i.e., $T \approx 300$ K. The formula and the required parameters for the approximation of g_R can be found in Jalali et al. (2006); Dimitropoulos et al. (2003); Ralston and Chang (1970); Renucci et al. (1975).

As indicated by Eq. (16), the entries of the Raman susceptibility consist of two contributions, $X_1^{ijkl}(f_2 - f_1)$ and $X_1^{ijkl}(f_2 - f_3)$. This can be derived from the fact that there exist two potential ways to promote atoms from the ground state to a higher vibrational eigenstate. Figure 1 illustrates the Raman process $f_0 = f_1 - f_2 + f_3$ in the special case of resonance. A photon of energy $hf_{1,3}$ excites the atom from the ground state to a virtual energy state E'_1 . Then, stimulated by a photon of frequency f_2 , part of the energy is used to promote the atom to the vibrational eigenstate $E_v = hf_v$, the other part is emitted as a photon with frequency f_2 . Thus, photons with energy $hf_{1,3}$ can be understood as the driving force for providing atoms to the vibrational eigenstate E_v . If a photon of energy $hf_{3,1}$ is absorbed by an atom located at the vibrational eigenstate E_v , the atom is excited to the virtual state E'_2 and falls back to the ground state immediately while emitting a photon of frequency f_0 . Considering f_1 as the frequency that implicitly provides atoms to the vibrational eigenstate, X_1^{ijkl} is differently pronounced depending on how precisely the resonance frequency f_v is hit by the frequency difference $f_1 - f_2$. In the case of resonance, i.e., $f_1 - f_2 = f_v$, the maximal value of X_1^{ijkl} is obtained. Analogously, X_2^{ijkl} considers the possibility of resonance between f_2 and f_3 , by regarding f_3 as the frequency that implicitly supplies atoms to the vibrational eigenstate.

4 Numerical implementation

In our simulation, we launch three waves (two pumps and one signal) with discrete frequencies into an SOI waveguide. By linear MC, waves at all frequencies couple into all

Fig. 1 Energy-diagram of the possible Raman processes in resonance. Virtual states, represented by the dashed lines, can only be used as transitions and cannot be occupied in contrast to eigenstates

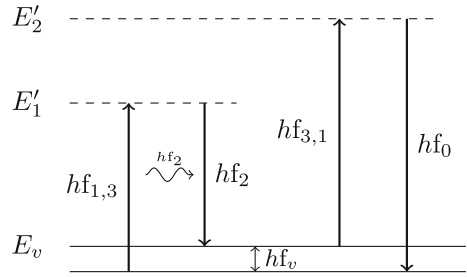


Table 1 The considered set of coupled differential equations which has to be solved simultaneously

	f_{P1}	f_{P2}	f_S	f_{OPC}	f_{BS}
$a = TE_0$	$\partial_z \hat{E}_{f_{P1}}^{(TE_0)}$	$\partial_z \hat{E}_{f_{P2}}^{(TE_0)}$	$\partial_z \hat{E}_{f_S}^{(TE_0)}$	$\partial_z \hat{E}_{f_{OPC}}^{(TE_0)}$	$\partial_z \hat{E}_{f_{BS}}^{(TE_0)}$
$a = TE_1$	$\partial_z \hat{E}_{f_{P1}}^{(TE_1)}$	$\partial_z \hat{E}_{f_{P2}}^{(TE_1)}$	$\partial_z \hat{E}_{f_S}^{(TE_1)}$	$\partial_z \hat{E}_{f_{OPC}}^{(TE_1)}$	$\partial_z \hat{E}_{f_{BS}}^{(TE_1)}$
$a = TE_2$	$\partial_z \hat{E}_{f_{P1}}^{(TE_2)}$	$\partial_z \hat{E}_{f_{P2}}^{(TE_2)}$	$\partial_z \hat{E}_{f_S}^{(TE_2)}$	$\partial_z \hat{E}_{f_{OPC}}^{(TE_2)}$	$\partial_z \hat{E}_{f_{BS}}^{(TE_2)}$

available modes at the same frequencies. Due to the nonlinear interaction, waves at all possible frequency combinations are generated in all available modes. Both interactions occur differently pronounced depending on phase mismatches $\Delta\beta_{lin}$ and $\Delta\beta$ and coefficients C and N . Consequently, the number of possible combinations for interaction quickly rises. We limit the simulation by only considering light propagation in the guided modes of the waveguide (TE_0, TE_1, TE_2) and by only taking frequencies into account that will be generated with non-negligible efficiency. Thus, the frequencies of the three input waves, i.e., f_{P1}, f_{P2}, f_S , and the two generated frequencies $f_{BS} = -f_{P1} + f_S + f_{P2}$ and $f_{OPC} = +f_{P1} - f_S + f_{P2}$ (arising from the BS and OPC FWM processes) are considered. Although this limitation drastically reduces complexity, still 15 coupled differential equations have to be solved simultaneously as summarized in Table 1.

The transversal field distributions $\vec{\Psi}_{f_i}^{(m)}$ and their corresponding propagation constants $\beta_{f_i}^{(m)}$ for the considered waveguide were calculated with an own full-vectorial mode solver based on Fallahkhair et al. (2008). After determining the required $\vec{X}^{\leftrightarrow[3]}$ (f_ζ, f_η, f_ρ) (for all possible frequency combinations accounting to f_i), the nonlinear coupling coefficients $N_{(m_1, m_2, m_3)}^{(a)}$ can be calculated. The influence of linear coupling and thus the magnitude of the linear coupling coefficients $C_{(m)}^{(a)}$ is determined by the coupling matrix $\delta\epsilon_r$ which models deviations from the unperturbed refractive index profile, e.g., caused by waveguide roughness or mechanical stress. Since $\delta\epsilon_r$ depends on various factors it is difficult to find analytic expressions for its entries. Therefore, a heuristic approach is often preferred that uses $\delta\epsilon_r$ to match the simulation and measurement results of linear coupling.

We numerically integrate the system of coupled differential equations (Eq. (13)) based on the third-order susceptibility (Sect. 3) with a variable order, variable step-size Adams-Bashforth-Moulton solver (ode113).

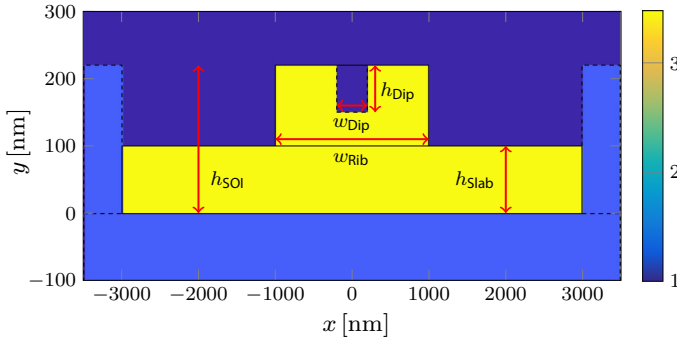


Fig. 2 Refractive index geometry of the nano-rib waveguide with slab, SOI and dip heights, as well as rib and dip widths

Table 2 Simulation (I) parameters: wavelengths and modes of propagating waves with high conversion efficiency as well as input powers and mode-dependent attenuation coefficients. The asterisk at I_{OPC}^* indicates that PM was optimized for the OPC process

	Input [nm]			Generated [nm]		Input power [dBm]			α [dB cm ⁻¹]
	P ₁	P ₂	S	I _{OPC} [*]	I _{BS}	P ₁	P ₂	S	
TE ₀									1
TE ₁		1535		1519	1529		20		2
TE ₂	1524		1540			20		10	3

5 Idler evolution in an SOI waveguide

5.1 Simulation (I)

First, an SOI waveguide with rib width 1800 nm, slab height 100 nm, SOI height 220 nm, propagation length 2 cm and one dip of width 400 nm and depth 70 nm is considered. Figure 2 shows the waveguide’s geometry, which is the same as in Kernetzky et al. (2020).

Table 2 summarizes the input/output wavelengths and their corresponding modes, optimized for best efficiency of the OPC process. We select realistic values for input powers, and mode-dependent attenuation coefficients, which are also included in Table 2. The resulting power evolution along the waveguide—without linear MC ($C = 0$)—is shown in Fig. 3a. It can be seen, that the propagation of the input waves (marked as \square , \star and \diamond) is dominated by the linear waveguide attenuation; the power decrease caused by the nonlinear power transfer to the OPC and BS idler is hardly visible in the log-domain. The OPC process (\rightarrow) with best PM is created with highest efficiency, while the BS process (\rightarrow) with slightly worse PM is created with less efficiency. The additional decrease in BS idler power compared to the OPC idler is caused by the larger phase mismatch $\Delta\beta$. All other potential FWM products at other modes and frequencies are not shown, since they are highly phase-mismatched, and thus have negligible power.

For the analysis of MC, we heuristically set

$$\delta\epsilon_r = \begin{bmatrix} 1 & 0 & 0 \\ 0 & 0 & 0 \\ 0 & 0 & 0 \end{bmatrix}$$

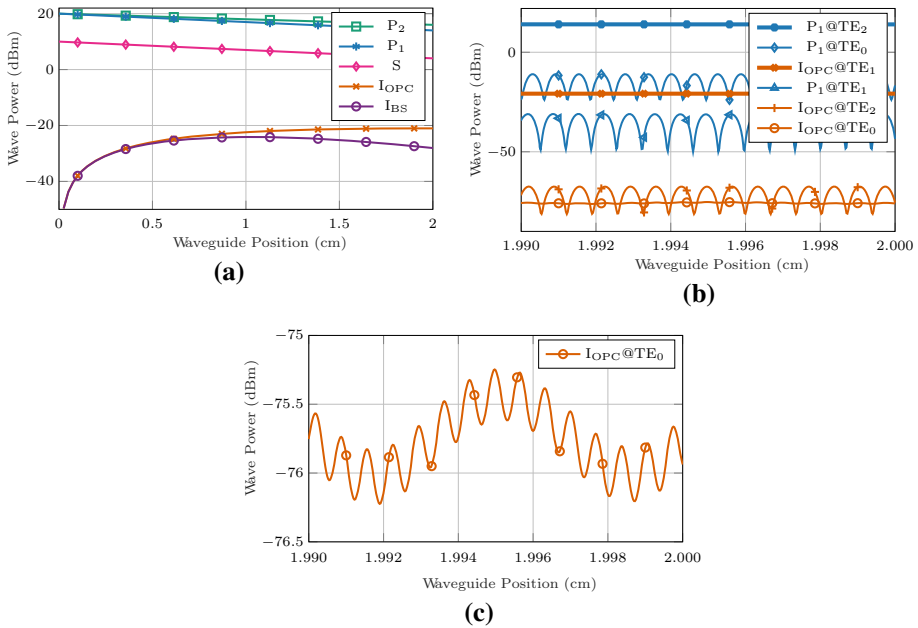


Fig. 3 **a** Simulated power evolution of pumps, signal and idlers along the waveguide without linear MC. The mode distribution is corresponding to Table 2. **b** Simulated power evolution of selected waves with linear and nonlinear coupling. **c** Vertical zoom on the OPC idler in TE₀ in (b)

to introduce MC. This breaks the orthogonality of modes in the computation of C in Eq. 14, by not taking into account the small but non-negligible y and z components of the transversal field profiles. We emphasize again, that more meaningful entries in this matrix need to be found by matching simulation with experimental data.

Figure 3b shows the power evolution with additional linear MC. In principle, all waves couple into all considered modes. We exemplarily show one pump and one idler (—, —). The oscillation periods depend on the corresponding $\Delta\beta_{lin}$ values as $L_{Oscillation} = \frac{2\pi}{|\Delta\beta_{lin}|}$ and the coupled powers on both, C and $\Delta\beta_{lin}$. For instance, the magnitude of the normalized coupling coefficient of the OPC idler from TE₁ to TE₀ (—○) is $|C_{(TE_1)}^{(TE_0)}| / \iint |\tilde{\Psi}_{f_{OPC}}^{(TE_0)}|^2 dA = 1.3 \times 10^{-4}$, whereas from TE₁ to TE₂ (—→) it is $|C_{(TE_1)}^{(TE_2)}| / \iint |\tilde{\Psi}_{f_{OPC}}^{(TE_2)}|^2 dA = 3.6 \times 10^{-3}$. The corresponding phase mismatches $|\Delta\beta_{lin}|$ are $|\beta_{f_{OPC}}^{(TE_1)} - \beta_{f_{OPC}}^{(TE_0)}| = 9.1 \times 10^4 \text{ m}^{-1}$ (—○), and $|\beta_{f_{OPC}}^{(TE_1)} - \beta_{f_{OPC}}^{(TE_2)}| = 9.2 \times 10^5 \text{ m}^{-1}$ (—→), respectively. While the coupling coefficient C from TE₁ to TE₂ is greater than from TE₁ to TE₀ (large values induce more coupled power), the phase mismatch $\Delta\beta_{lin}$ from TE₁ to TE₂ is also greater than from TE₁ to TE₀ (large values induce less coupled power). This leads to similar power levels of the OPC idler in TE₀ and TE₂ (—○, —→). Figure 3c shows a closeup of I_{OPC} in mode TE₀ and reveals two oscillations. The slower one with period of roughly the plotted range is caused by direct coupling from TE₁. The fast oscillation arises from second-order linear coupling from TE₂ and is therefore only weakly pronounced.

Table 3 Simulation (II) parameters: wavelengths and modes of propagating waves with high conversion efficiency as well as input powers and mode-dependent attenuation coefficients. The asterisk at I_{BS}^* indicates that PM was optimized for the BS process

	Input [nm]			Generated [nm]		Input power [dBm]			α [dB cm ⁻¹]
	P ₁	P ₂	S	I _{OPC} *	I _{BS}	P ₁	P ₂	S	
TE ₀	1300			1296.57	1303.44	19.33			0.9
TE ₁		1540	1544.84				23.95	11.28	1.8
TE ₂									1.8

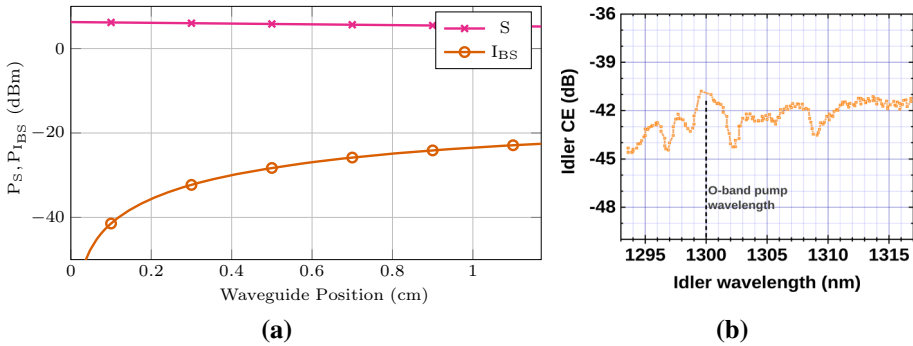


Fig. 4 **a** Simulated BS idler and signal power evolution. The mode distribution is corresponding to Table 2. **b** Measured CE output of the SOI waveguide, from Ronniger et al. (2021)

5.2 Simulation (II) with experimental verification

For verifying the simulation results we use measured data from an SOI waveguide with rib width 1672 nm, slab height 100 nm, SOI height 220 nm, and propagation length 11.3 mm (Ronniger et al. (2021); Kernetzky et al. (2021)). Table 3 summarizes the simulation parameters optimized for best efficiency of the BS process.

Since mode multiplexer and grating coupler at the input and output of the waveguide are lossy, the simulation parameters have to be adjusted accordingly which is reflected in a reduced input power, i.e., $P_{P_1} = 13.92$ dBm, $P_{P_2} = 18.75$ dBm, and $P_S = 6.28$ dBm. A suitable means to evaluate the generation process of the BS idler is the input-output conversion efficiency (CE): $CE = P_{I_{BS}}/P_S$ (or $CE = P_{I_{BS}} - P_S$ in log-domain), where the signal and idler power is defined at the input (before mode multiplexer and grating coupler) and at the output (after mode demultiplexer and grating coupler) of the chip, respectively. Figure 4a shows that the simulated idler power is $P_{I_{BS}} = -22.5$ dBm at the end of the waveguide. This results in a CE of $CE_{sim} = -22.5$ dBm - 5 dB - 11.28 dBm \approx -39 dB, where -5 dB includes the losses caused by demultiplexer and grating coupler at the output. From Fig. 4b, the measured CE for $\lambda_{I_{BS}} = 1303.44$ nm is $CE_{meas} \approx$ -42 dB. This is a very good match between measurement and simulation, since the remaining CE difference of 3 dB is very small considering measurement imperfections, material parameter, temperature variations, etc.

6 Conclusions

We modeled electronic and molecular parts $\vec{\chi}_e$ and $\vec{\chi}_R$ of the silicon susceptibility $\vec{\chi}^{[3]}$. We linked the components of $\vec{\chi}_e$ to material parameters and presented a closed-form solution for $\vec{\chi}_R$. Although the approximations we applied limit the usable wavelength region, they are valid for commonly used optical transmission bands.

We derived and numerically integrated a set of coupled differential equations, which model linear and nonlinear light evolution along waveguides. Each frequency component in each mode is modeled by an equation that includes linear attenuation, linear MC, and FWM nonlinearity caused by the material susceptibility $\vec{\chi}^{[3]}$. We verified the validity of the proposed model by measured data of an SOI waveguide.

Acknowledgements This work was supported by the DFG project HA 6010/6-1.

Funding Open Access funding enabled and organized by Projekt DEAL.

Open Access This article is licensed under a Creative Commons Attribution 4.0 International License, which permits use, sharing, adaptation, distribution and reproduction in any medium or format, as long as you give appropriate credit to the original author(s) and the source, provide a link to the Creative Commons licence, and indicate if changes were made. The images or other third party material in this article are included in the article's Creative Commons licence, unless indicated otherwise in a credit line to the material. If material is not included in the article's Creative Commons licence and your intended use is not permitted by statutory regulation or exceeds the permitted use, you will need to obtain permission directly from the copyright holder. To view a copy of this licence, visit <http://creativecommons.org/licenses/by/4.0/>.

References

- Agrawal, G.P.: *Nonlinear Fiber Opt.* Elsevier/Academic Press, Amsterdam (2013)
- Boyd, R.W.: *Nonlinear optics.* Elsevier, Amsterdam (2003)
- Bristow, A.D., Rotenberg, N., Van Driel, H.M.: Two-photon absorption and Kerr coefficients of silicon for 850–2200 nm. *Appl. Phys. Lett.* **90**(19), 191104 (2007)
- Dimitropoulos, D., Claps, R., Han, Y., Jalali, B.: Nonlinear optics in silicon waveguides: stimulated Raman scattering and two-photon absorption. In: *Integrated Optics: Devices, Materials, and Technologies VII*, vol. 4987. International Society for Optics and Photonics, (2003), pp. 140–148
- Dimitropoulos, D., Houshmand, B., Claps, R., Jalali, B.: Coupled-mode theory of the Raman effect in silicon-on-insulator waveguides. *Opt. Lett.* **28**(20), 1954–1956 (2003)
- Fallahkhaier, A.B., Li, K.S., Murphy, T.E.: Vector finite difference modesolver for anisotropic dielectric waveguides. *J. Lightwave Technol.* **26**, 1423–1431 (2008)
- Gajda, A., Da Ros, F., da Silva, E. P., Peczek, A., Liebig, E., Mai, A., Galili, M., Oxenløwe, L. K., Petermann, K., Zimmermann, L.: Silicon waveguide with lateral p-i-n diode for nonlinearity compensation by on-chip optical phase conjugation. In: *Optical Fiber Communication Conference. Optical Society of America* (2018)
- Höfler, U., Kernetzky, T., Hanik, N.: Modeling material susceptibility in silicon for four-wave mixing based nonlinear optics. In: *International Conference on Numerical Simulation of Optoelectronic Devices (NUSOD)*, 9 (2021)
- Hon, N.K., Soref, R., Jalali, B.: The third-order nonlinear optical coefficients of Si, Ge, and Si_{1-x}Ge_x in the midwave and longwave infrared. *J. Appl. Phys.* **110**(1), 9 (2011)
- Jalali, B., Raghunathan, V., Dimitropoulos, D., Boyraz, O.: Raman-based silicon photonics. *IEEE J. Select. Topics Quantum Electron.* **12**(3), 412–421 (2006)
- Kernetzky, T., Jia, Y., Hanik, N.: Multi dimensional optimization of phase matching in multimode silicon nano-rib waveguides. In: *Photonic Networks; 21st ITG-Symposium, Leipzig, Germany* (2020)

- Kernetzky, T., Ronniger, G., Höfler, U., Zimmermann, L., Hanik, N.: Numerical optimization and CW measurements of SOI waveguides for ultra-broadband C-to-O-band conversion. In: 2021 The European Conference on Optical Communication (ECOC), Bordeaux, France, 9 (2021)
- Lin, Q., Painter, O.J., Agrawal, G.P.: Nonlinear optical phenomena in silicon waveguides: modeling and applications. *Opt. Express* **15**(25), 604–644 (2007)
- Minzioni, P., Pusino, V., Cristiani, I., Marazzi, L., Martinelli, M., Langrock, C., Fejer, M.M., Degiorgio, V.: Optical phase conjugation in phase-modulated transmission systems: experimental comparison of different nonlinearity-compensation methods. *Opt. Express* **18**, 18119 (2010)
- Osgood, R., Panoiu, N., Dadap, J., Liu, X., Chen, X., Hsieh, I.-W., Dulkeith, E., Green, W., Vlasov, Y.A.: Engineering nonlinearities in nanoscale optical systems: physics and applications in dispersion-engineered silicon nanophotonic wires. *Adv. Opt. Photon.* **1**(1), 162–235 (2009)
- Rademacher, G., Luis, R.S., Puttnam, B.J., Awaji, Y., Suzuki, M., Hasegawa, T., Furukawa, H., Wada, N.: Wideband intermodal nonlinear signal processing with a highly nonlinear few-mode fiber. *IEEE J. Sel. Topics Quantum Electron.* **26**, 1–7 (2020)
- Ralston, J., Chang, R.: Spontaneous-Raman-scattering efficiency and stimulated scattering in silicon. *Phys. Rev. B* **2**(6), 1858 (1970)
- Renucci, J., Tyte, R., Cardona, M.: Resonant Raman scattering in silicon. *Phys. Rev. B* **11**(10), 3885 (1975)
- Ronniger, G., Lischke, S., Mai, C., Zimmermann, L., Petermann, K.: Investigation of inter-modal four wave mixing in p-i-n diode assisted SOI waveguides. In: IEEE Photonics Society Summer Topicals Meeting Series (SUM). Cabo San Lucas, Mexico: IEEE **2020**, 1–2 (2020)
- Ronniger, G., Sackey, I., Kernetzky, T., Höfler, U., Mai, C., Schubert, C., Hanik, N., Zimmermann, L., Freund, R., Petermann, K.: Efficient ultra-broadband C-to-O band converter based on multi-mode silicon-on-insulator waveguides. In: 2021 The European Conference on Optical Communication (ECOC), Bordeaux, France, 9 (2021)
- Vukovic, D., Schröder, J., Da Ros, F., Du, L.B., Chae, C.J., Choi, D.-Y., Pelusi, M.D., Peucheret, C.: Multi-channel nonlinear distortion compensation using optical phase conjugation in a silicon nanowire. *Opt. Express* **23**, 3640 (2015)
- Zhang, J., Lin, Q., Piredda, G., Boyd, R., Agrawal, G., Fauchet, P.: Anisotropic nonlinear response of silicon in the near-infrared region. *Appl. Phys. Lett.* **91**(7), 071113 (2007)

Publisher's Note Springer Nature remains neutral with regard to jurisdictional claims in published maps and institutional affiliations.